Tuning magnetism in graphene nanoribbons via strain and adatoms

Pablo Moles [1,*] Hernán Santos [2,3,†] Francisco Domínguez-Adame [1] and Leonor Chico [1]

[1]GISC, Departamento de Física de Materiales, Facultad de Ciencias Físicas, Universidad Complutense, E-28040 Madrid, Spain

[2]Departamento de Física, Facultad de Ciencias Ambientales y Bioquímica, Universidad de Castilla-La Mancha, Campus Tecnológico de la Fábrica de Armas, Avenida Carlos III s/n, 45071 Toledo, Spain

[3]Departamento de Matemática Aplicada, Ciencia e Ingeniería de Materiales y Tecnología Electrónica, ESCET, Universidad Rey Juan Carlos, C/ Tulipán s/n, Móstoles 28933, Madrid, Spain

(Received 12 March 2025; accepted 14 August 2025; published 15 September 2025)

We investigate the impact of strain and adsorbed H adatoms on the magnetic properties of zigzag graphene nanoribbons (ZGNRs) using a combination of tight-binding and density functional theory methods for both ferromagnetic (FM) and antiferromagnetic (AFM) edge configurations. We focus on the metallic FM edge configuration of the ZGNRs to better exploit the tuning of its properties. We find that the magnetic configuration of H adatoms is strongly influenced by the edges, with an AFM coupling between edges and the H adatom. In fact, the magnetic spatial pattern of the H adatom differs from that found in graphene due to this edge coupling. Importantly, we find robust discrete plateaus of integer magnetic moment as strain is varied in the defected ZGNRs, which we relate to changes in the band structure, namely, a half-metallic character or the opening of a gap. This behavior can be of interest for magnetic applications of carbon-based nanostructures.

DOI: 10.1103/6tny-vt8q

I. INTRODUCTION

Partially filled d and f orbitals are responsible for the magnetic order of transition metals and rare earth ions in common magnetic materials. However, their environmentally harmful nature has boosted the quest of alternative routes to achieve magnetic order in solids. In this context, p-orbital magnetism has arisen in the last two decades as a possible way to realize sustainable spintronic devices [1]. It can emerge in low-dimensional carbon-based materials such as nanostructured graphene, nanoflakes, or nanoribbons. At the edges or vacancies of such nanomaterials, the p_z orbitals of carbon atoms give rise to π-electronic states, in which electron-electron interactions induce magnetic ordering, referred to as π magnetism [2,3].

Magnetic graphene nanostructures are particularly promising for spintronics [4,5]. Graphene exhibits weak spin-orbit and hyperfine couplings [6–8], which are the main physical mechanisms for relaxation and decoherence of electron spins. This, in addition to the high electron mobility in this material, results in the longest spin diffusion length achieved at room temperature [9]. These characteristics are fundamental for the application of graphene-based materials in spintronic devices.

Bulk pristine graphene is intrinsically nonmagnetic. However, there are two main scenarios in which magnetism may emerge in this material. The first one is related to the presence of point defects in the graphene lattice, specifically vacancies and adatoms [2]. This type of magnetism has been extensively studied [10–12] and experimentally observed in irradiated graphite samples [13–15]. While these early studies lacked precision over the distribution of defects, advancements in experimental techniques have allowed for the controlled creation of defects. The adsorption of adatoms, particularly hydrogen, represents one of the most effective methods for modulating the magnetic properties in graphene with atomic precision [16]. The second scenario involves certain graphene nanostructures, namely, graphene nanoflakes [2] and zigzag graphene nanoribbons (ZGNRs), which present intrinsic magnetic ordering without the need of other defects than the edges. As it is well known, these nanoribbons develop low-energy states localized at the zigzag edges [17,18], which are predicted to be spin polarized due to electron-electron interactions [19–21]. ZGNRs can present half-metallicity, producing fully spin-polarized currents [22]. Moreover, magnetoresistive devices [23], spin valves [24], spin diodes [25], and field-effect transistors [26] based on ZGNRs have been proposed to exploit their magnetic edge states, constituting the building blocks of prospective graphene-based spintronics.

The lack of atomic precision in early synthesis methods of ZGNRs, such as solution-phase chemistry [27] or top-down approaches [28], hampered the experimental verification of magnetism in these systems, mainly because magnetic ordering is very sensitive to edge roughness [29]. However, the development of on-surface synthesis techniques for ZGNRs has provided the observation of energy gaps and local density of states consistent with the existence of edge magnetism [30]. Although the direct experimental evidence of magnetism in ZGNRs still remains elusive [31], the atomic precision achieved both in synthesis and in defect creation in graphene

*Contact author: pmoles@ucm.es
†Contact author: Hernan.Santos@uclm.es

nanostructures is a powerful motivation to explore the interplay of these two sources of magnetism in ZGNRs and the possible ways to modify it [32].

Another way to tune the electronic and magnetic properties of pristine graphene and graphene nanosystems, such as nanoribbons, is by means of strain. This method to modify the physical properties of a material has been proved to be effective and tunable, originating the term straintronics [33]. With respect to graphene, a gap may open [34], and pseudomagnetic fields due to strain give rise to valley-polarized states [35,36]. In ZGNRs, either flat or helicoidal, mechanical deformations have an impact on their magnetic properties. However, few studies have explored this effect. In flat ZGNRs, an increase of the magnetic susceptibility with applied strain in pristine samples has been reported [37]. Nevertheless, its consequences on the electronic structure, such as changes in the band structure and electronic distribution, were not been addressed therein, and a more comprehensive understanding is still lacking. Also, helicoidal ZGNRs have been recently shown to present fully polarized edge states [38], although this geometry presents structural difficulties for practical applications compared to their flat counterparts. To the best of our knowledge, the interplay between edge magnetism and localized magnetic moments induced by point defects, such as vacancies or hydrogen adsorption, located *inside* the ribbon at finite distances from the edges (edge-point defect interaction), remains largely unexplored. Even less attention has been devoted to the possibility of modulating this nontrivial magnetic coupling via mechanical strain. These are the focal points of the present study.

In this work, we explore the strain tunability of the magnetic response of ZGNRs via the presence of point defects, namely, adsorbed H atoms, located inside the ribbon. Note that we do not consider defects located at the edge, which amount to an edge modification, as reported in Ref. [32], nor reconstructed vacancies, such as those studied in Ref. [39]. In fact, we are interested in systems without the sublattice mixing produced by the reconstruction, with a net magnetic moment, where a controlled defect engineering can be achieved via adsorption, avoiding random disorder or uncontrolled defects. We will mainly focus on the ferromagnetic (FM) edge configuration, which we find to be optimal for achieving tunability.

In order to elucidate the origin of the physical responses found, we first analyze the role of induced strain as a way to modify the electronic properties of ZGNRs [33,40]. Using first-principles and tight-binding (TB) methods, we consider uniaxial strain along the zigzag direction of a ZGNR, resulting in a smooth, albeit important, enhancement of its magnetic response. We attribute this increase to modifications in the band structure produced by the strain field. Second, we investigate the role of adsorbed H atoms and its coupling to the edge states of the ZGNRs, modifying its properties via strain. With these previous studies at hand, we are in the position to explore the optimal scenario for the tuning of magnetic properties. For the FM configuration, we find that the magnetic moment varies with strain yielding robust discrete integer plateaus in the defected ZGNRs. These plateaus can be explained by resorting to the band structure, being related to the half-metallic character of the gap opening with strain,

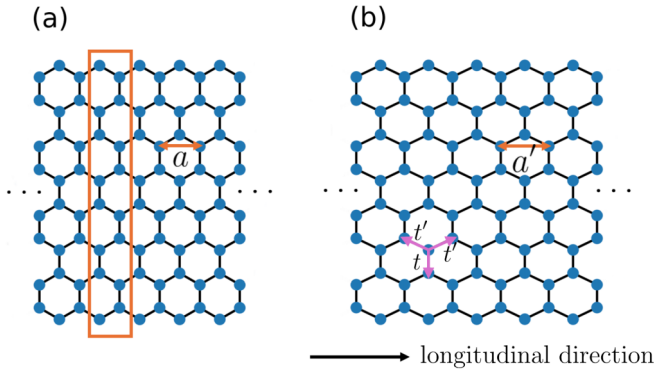

FIG. 1. (a) Atomic arrangement of an unstrained 8-ZGNR. The unit cell and the lattice parameter are displayed. (b) The same ZGNR with induced longitudinal strain. The strain-modified lattice and hopping parameters are also shown.

which can be relevant for magnetic applications of graphene nanoribbons. Additionally, we have verified that the Anderson impurity model gives an excellent description of the H adatom, much better than the commonly employed vacancy model, yielding an excellent agreement with *ab initio* results. We consider that these results clarify the nature of edge-point defect coupling and provide another avenue to change in a detectable, stepwise fashion, the magnetic properties of these systems.

The article is organized as follows. Section II describes the system under consideration and outlines the computational methods employed. Specifically, we detail the tight-binding model in Sec. II A and the density functional theory (DFT) calculations in Sec. II B. Our results are presented in Sec. III, divided into three main parts. First, Sec. III A investigates the effects of strain on pristine ZGNRs. Second, Sec. III B examines the adsorption of H adatoms, and finally, Sec. III C studies the role H adatoms in combination with strain on ZGNRs. Section IV concludes with a brief summary of our main findings.

II. SYSTEM AND COMPUTATIONAL METHODS

The system under consideration consists of an infinitely long ZGNR, with a lattice parameter $a = \sqrt{3}\,a_0$, $a_0 = 1.42$ Å being the C–C distance. We label the nanoribbon according to its width, W-ZGNR, where W indicates the number of zigzag chains of atoms across the width of the nanoribbon. Thus, the nanoribbon has $N = 2W$ C atoms in its translational unit cell [see Fig. 1(a) for further details].

We consider that a uniform and uniaxial strain is applied along the zigzag direction of the nanoribbon. The crystal structure of the nanoribbon is modified in this direction, altering the interatomic distances and thus the lattice parameter, denoted as a'. As further discussed later, we assume that the width of the ZNGR remains unchanged after uniaxial stress. Figure 1(b) shows this structural modification. For a ZGNR with this applied uniaxial strain, the size change corresponds directly to the modification of the lattice parameter in that direction. Thus, we quantify the strain as

$$\epsilon = \frac{a' - a}{a}. \tag{1}$$

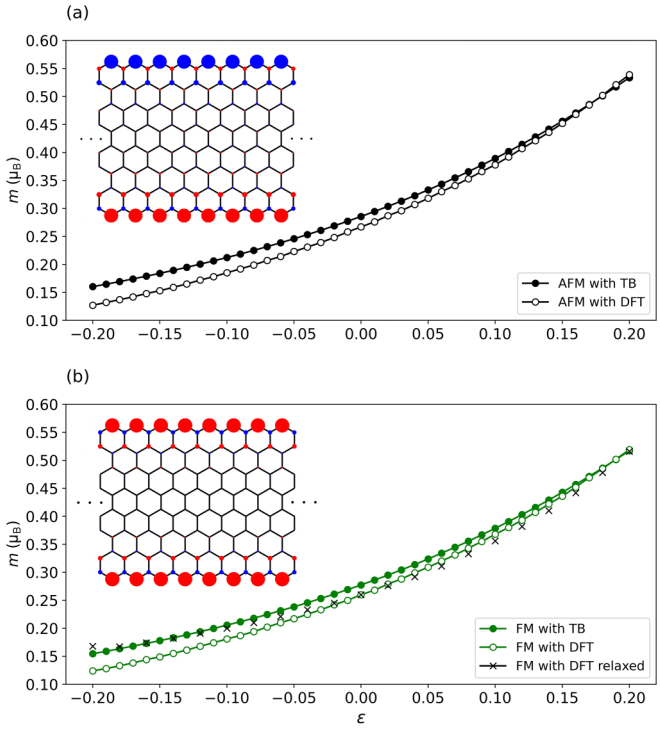

FIG. 2. Spatial distribution of the magnetic moments in a 8-ZGNR (radii of the circles are proportional to the magnetic moment at each site, with red circles indicating positive values and blue circles indicating negative ones) and value of the magnetic moment of the edge atoms as a function of strain in (a) the AFM configuration and (b) the FM configuration.

Admittedly, this assumption does not accurately describe the atomic rearrangement in a real situation, where the ZGNR would also be relaxed in the transverse direction due to the Poisson effect [40]. However, the Poisson effect is relatively small in graphene, with Poisson ratios ranging from 0.14 to 0.19 [41,42]. Furthermore, we have performed DFT calculations that account for Poisson relaxation (see details in Sec. II B) and found that it does not substantially alter the magnetic response [see Fig. 2(b)]. Consequently, we have chosen to focus on the simplified description, which aims to clarify the main underlying physics related to magnetism.

We also consider H adatoms adsorbed onto the ZGNR. It is well established that H adatoms form covalent bonds with C atoms, where the $1s$ H orbital hybridizes with the $2p_z$ C orbital. However, the presence of H adatoms does not lead to significant deformation of the graphene lattice. It only induces a slight out-of-plane relaxation in the surrounding region [2,10]. Our DFT calculations confirm that this relaxation does not result in noticeable changes of the electronic structure. Consequently, in this study, we neglect the out-of-plane relaxation when modeling the occurrence of H adatoms and focus on the magnetic changes induced in the system.

A. Tight-binding model

The TB approach followed in this work employs a one-orbital mean-field Hubbard model, a well-known and extensively used approximation to describe magnetism in carbon materials [2]. Its results have been demonstrated to be in good agreement with first-principles calculations [43–46]. The Hubbard model only considers the nonhybridized p_z orbital of each C atom, which contributes with one electron to the resulting π band. For undoped or unbiased graphene that we considered, the ZGNR is half filled. The Hamiltonian of the system splits into two parts, $\mathcal{H} = \mathcal{H}_0 + \mathcal{H}_U$, where $\mathcal{H}_0$ corresponds to the noninteracting TB Hamiltonian and $\mathcal{H}_U$ represents the electron-electron interaction. Here, the noninteracting TB Hamiltonian only includes nearest-neighbor couplings,

$$\mathcal{H}_0 = -\sum_{\langle i,j\rangle,\sigma} t'\, c^\dagger_{i,\sigma}\, c_{j,\sigma} + \text{H.c.}, \tag{2}$$

where H.c. stands for Hermitian conjugate and the summation in $\langle i, j\rangle$ runs over nearest-neighbor C atoms. The origin of energy is set at the energy of the p_z orbital. Here, $c^\dagger_i$ and c_j are the creation and annihilation fermion operators at atoms i and j, respectively. The parameter t' denotes the nearest-neighbor hopping energy and $\sigma = \uparrow, \downarrow$ indicates the electron spin.

In a TB model, the hopping parameter depends on the interatomic distance; in this case, it is altered due to the strain. Among the three possible first-neighbor hoppings, the transverse one remains unchanged, since the distance between atoms remains constant in this direction. However, the other two hoppings between bonds with a longitudinal component are modified due to the variation on the atomic separation in the direction of strain. We denote these as t' [see Fig. 1(b)]. We account for this effect by modifying the hopping parameters with the distance according to the expression [34]

$$t' = t\, e^{-\beta(r/a_0-1)}, \tag{3}$$

where $t = 2.5$ eV is the hopping in the strain-free case, r is the distance between the atoms, and $\beta = 3.1$. The parametrization (3) has been successfully validated with DFT results [47].

The magnetic response of the ZGNR is modeled with the second term of the Hamiltonian, $\mathcal{H}_U$. The Hubbard model introduces these interactions by means of an on-site Coulomb repulsion. Thus, electrons with opposite spin occupying the same site experience a repulsion quantified by the energy $U > 0$, known as the Hubbard parameter. The interaction Hamiltonian is

$$\mathcal{H}_U = U \sum_i n_{i,\uparrow} n_{i,\downarrow}, \tag{4}$$

where $n_{i,\sigma} = c^\dagger_{i,\sigma}\, c_{i,\sigma}$ is the number operator, which gives the spin-resolved electron density at atom i. We set the value of $U = 3$ eV in our numerical calculations. To deal with the many-body interaction Hamiltonian $\mathcal{H}_U$, the restricted Hartree-Fock mean-field approximation is adopted. The resulting Hamiltonian is approximated as

$$\mathcal{H}_U = U \sum_i (n_{i,\uparrow}\langle n_{i,\downarrow}\rangle + n_{i,\downarrow}\langle n_{i,\uparrow}\rangle - \langle n_{i,\uparrow}\rangle\langle n_{i,\downarrow}\rangle). \tag{5}$$

Here, the spin-up and spin-down matrix elements at site i depend on $\langle n_{i,\downarrow}\rangle$ and $\langle n_{i,\uparrow}\rangle$, respectively, which represent the average electron population with opposite spins at that site. These numbers are the expectation values of the spin-resolved electron densities obtained from the eigenvectors of

$\mathcal{H}$, which are initially unknown. The Hamiltonian is solved self-consistently, using the following procedure: Starting from an initial guess of $\langle n_{i,\sigma}\rangle$ chosen randomly, (1) the $2N \times 2N$ matrix representation of the Hamiltonian is obtained. (2) The Hamiltonian $\mathcal{H}(k)$ is diagonalized in the reciprocal space, and the corresponding spin-polarized eigenvectors $\phi_{v,i,\sigma}(k)$ are computed, where v is the band index. (3) The updated spin-resolved densities are obtained as follows:

$$\langle n_{i,\sigma}\rangle = \frac{1}{2\pi}\sum_{v=1}^{N}\int_{-\pi/a}^{\pi/a}\phi^{\dagger}_{v,i,\sigma}(k)\phi_{v,i,\sigma}(k)\,\mathrm{d}k, \tag{6}$$

where the summation runs up to the Nth band since the system is half filled. We employ a fine grid of 5000 k wave numbers over the Brillouin zone to perform the numerical integration in Eq. (6). Given the $\langle n_{i,\sigma}\rangle$ values, steps (1)–(3) are repeated iteratively until convergence is reached for the values of the electron densities. A more detailed explanation can be found in Ref. [48] for a similar self-consistent algorithm.

From the imbalance of the obtained spin-polarized densities of electrons, a local site-resolved magnetic moment arises:

$$m_i = \mu_B(\langle n_{i,\uparrow}\rangle - \langle n_{i,\downarrow}\rangle), \tag{7}$$

where μ_B is the Bohr magneton. Finally, the total magnetic moment per unit cell of the system is given by $M = \sum_i m_i$. We will present these magnitudes in Sec. III.

Finally, we employ the TB model to address the effect of hydrogen adsorption. A commonly used approach consists of substituting the H adatom by a single vacancy defect, neglecting lattice relaxation. This is motivated by the minimal lattice distortion produced by the H adatom and the hybridization of the C orbital, which effectively removes the orbital from the low-energy spectrum. These two factors make it possible to assume that a vacancy in an undistorted lattice is equivalent to an H adatom. Within this approximation, the vacancy is modeled as empty atomic site, removing the corresponding hopping terms in the electron Hamiltonian [12,46]. For comparison, we have also implemented a more realistic Anderson model, where the H adatom is treated as an impurity [49–51]. In this case, an additional term in the Hamiltonian is added to describe the impurity states and their interaction with the graphene lattice, given by

$$\mathcal{H}_{\mathrm{imp}} = U_H h^{\dagger}_{\uparrow}h_{\uparrow}h^{\dagger}_{\downarrow}h_{\downarrow} + \sum_{\sigma}\epsilon_H h^{\dagger}_{\sigma}h_{\sigma} - t_H\sum_{\sigma}(c^{\dagger}_{0,\sigma}h_{\sigma} + \mathrm{H.c.}), \tag{8}$$

where $h^{\dagger}_{\sigma}$ and h_{σ} are the creation and annihilation operators for an electron in the $1s$ orbital of the H adatom, respectively. The C atom bonded to the H adatom is located at the atomic site $i = 0$. We set the on-site energy $\epsilon_H = 1.7\,\mathrm{eV}$, the intra-atomic Coulomb repulsion $U_H = 1.3\,\mathrm{eV}$, and the hopping energy between the C and the H adatoms is set $t_H = 5.2\,\mathrm{eV}$. These values are obtained by fitting to our DFT calculations presented below.

B. First-principles calculations

We have performed first-principles calculations within the DFT framework using the SIESTA code with spin polarization [52]. The crystal structures were optimized with the revised Perdew-Burke-Ernzerhof functional [53]. The electron-ion interactions are modeled with norm-conserving nonlocal Troullier-Martins pseudopotentials described with a double-ζ singly polarized basis set. The energy cutoff is set to 400 Ry. The structure was relaxed by conjugate gradient optimization until forces were smaller than 0.005 eV/Å. This provides enough precision to obtain reliable strain properties. Periodic boundary conditions were applied along the longitudinal axis of the ZGNR, so we use sufficiently large supercell parameters (20 Å) in the perpendicular and transverse directions to prevent spurious interactions between adjacent nanoribbons. All C atoms at the edges were passivated by hydrogen. Finally, we have employed a Monkhorst-Pack scheme with $n \times 1 \times 1$ k points sampling of the Brillouin zone, where n is set to 5000 k points. This large number is essential to avoid a nonphysical magnetic response of the nanoribbon.

To obtain the strain properties, we employ the following scheme: (1) We perform a fully relaxed calculation with the FM and antiferromagnetic (AFM) guess configurations for each ZGNR. (2) From the relaxed structure, we apply strain to the supercell along the longitudinal direction. (3) To check how to address the transverse strain, we perform a relaxation on the transversal direction. This allows us to widen or narrow the nanoribbon depending on the compressive or tensile strain induced along the longitudinal direction. In this way, elastic properties such as the Poisson ratio can be obtained. In each case, we extract the total magnetic moments from the Mulliken spin-split populations for each orbital and atom.

III. RESULTS

In order to clarify the effect of point defects in strained ZGNRs, we analyze first the role of strain separately, in both FM and the AFM solutions. This allows us to highlight the impact of atom adsorption in these systems, assess the changes induced by the point defects, and elucidate the origin of the observed effects.

The maximum strain that graphene can withstand is approximately 25%, according to both theoretical [41,54] and experimental [55,56] studies. In our study, we primarily consider strain values up to 20%, unless stated otherwise. It is worth mentioning that most experiments make use of local probe microscopes to induce strain in graphene. Previous numerical studies revealed breaking of valley degeneracy due to a nonuniform strain produced by out-of-plane deformation [35,36]. However, in this work we assume uniform strain and neglect valley polarization.

A. Strain on pristine ZGNRs

The Hubbard model predicts two possible magnetic solutions in a ZGNR depending on the relative orientation of spins at opposite edges. Due to the strong coupling between neighboring atoms, the spins within an edge are ferromagnetically coupled. However, edge-to-edge interaction is weaker and decays as $1/W^2$ with the ribbon width W, so two solutions can be explored. When the spins on one edge are antiparallel to those on the opposite edge, the solution is AFM, as depicted in Fig. 2(a). If the spins at both edges are parallel, the solution is FM, as shown in Fig. 2(b). An analysis of the total

energy of both configurations reveals that the AFM solution is the ground state. However, since the energy difference with respect to the FM state is only a few meV even for narrow ribbons ($W = 8$) as those studied here [19], it is easy to switch between the two configurations, for instance, by flipping the spins with a small magnetic field [23]. Therefore, in view of this, we study both AFM and FM states.

In Fig. 2, we show the magnetic moment of the C atoms at the edges as a function of strain for the AFM and FM configurations. The edge atoms are the most relevant, since they provide the main contribution to the total magnetic moment. Positive (tensile) and negative (compressive) strain values are considered, following Eq. (1). Note that compressive strain in graphene usually produces out-of-plane deformations like ripples or bending; for the sake of clarity, these effects are not considered in this work. The magnetic moments are computed using both the TB approach and DFT calculations. The edge magnetic moment is found to increase gradually and smoothly with strain, presenting the same trend in both magnetic configurations. It increases by 41% (42%) with respect to the strain-free situation when the strain is +0.10 in the AFM (FM) configuration, according to DFT results. For an induced strain of +0.20, the magnetic moment is 102% (101%) higher than the strain-free ZGNR in the AFM (FM) configuration. This effect shows that the magnetic response of a strained ZGNR can be selectively enhanced.

The excellent agreement between the TB and DFT results in Fig. 2 is remarkable. The difference is slightly higher in the case of compressive strain, but this condition is less common in actual experiments. For tensile strains, the maximum difference between both methods arises in strain-free samples and corresponds to a deviation in magnetic moment of 7.1% and 6.5% in Figs. 2(a) and 2(b), respectively. Furthermore, using DFT we examine the effect of the relaxation in the transverse direction due to the Poisson effect in the FM configuration [see black crosses in Fig. 2(b)]. Interestingly, there is no significant difference between this result and the nonrelaxed situation. For instance, the magnetic moment differs only by 6.1% between the relaxed and the TB nonrelaxed cases when the strain is +0.10. This demonstrates the validity of our assumption that relaxation effects are negligible.

We also study how the magnetic moment varies with the width of the ZGNR. Figure 3 depicts the edge magnetic moment plotted against the width expressed in number of zigzag chains W, for the strain-free and +0.10 strain cases. The AFM solution yields slightly higher values than the FM solution when the ZGNR is narrow. In both cases, the magnetic moment increases as the width increases. The TB calculations enable us to explore very wide ZGNRs, where the magnetic moment reaches saturation, with both the AFM and FM solutions converging to the same value. Additionally, the results obtained with DFT for narrow ZGNRs are also shown for comparison. However, scaling to large widths with this approach is time-consuming. In such cases, the TB model offers a much more efficient way to obtain reliable results in the case of wide ZGNRs.

To elucidate the enhancement of the magnetic moment with strain observed in Fig. 2, we analyze the band dispersions of the 8-ZGNR. Figure 4 shows the band structures for the AFM configuration with both the TB (solid line) and

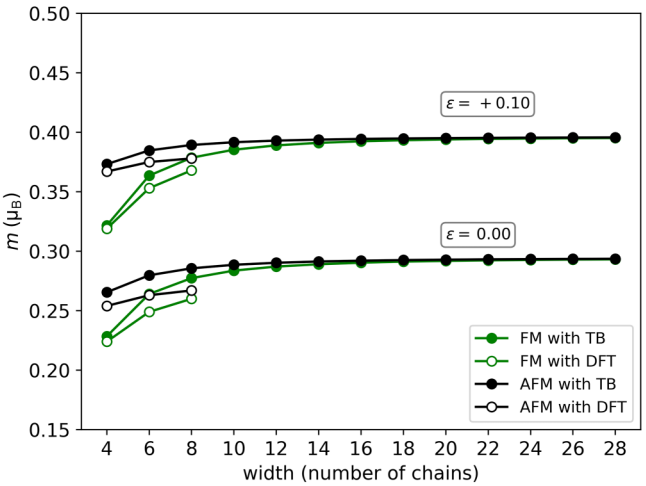

FIG. 3. Magnetic moment of the edge atoms against the width W of the ZGNR. The graph includes data for two strain values, 0.00 and +0.10.

DFT (dotted line) approaches for two strain values. In the AFM configuration, up and down spin-polarized bands are degenerate, and a gap opens between the edge bands. The edge states open a gap, with the Fermi level in between. Figure 4(a) corresponds to the strain-free case, while Fig. 4(b) shows the behavior when the ZGNR is subjected to +0.10 strain. Strain does not change the overall aspect of the bands. However, two differences are apparent. First, the bands become significantly flatter with strain, as expected, since the bandwidth is proportional to the hopping parameter and this decreases with increasing distance between C atoms. Second, the portion of the band edge states that exhibits flat character becomes larger compared to the dispersive region of the band, extending over a wider range of momentum in the Brillouin zone. As a consequence, a larger number of the states of the band are edge-localized, leading to an enhancement of the edge magnetic moment.

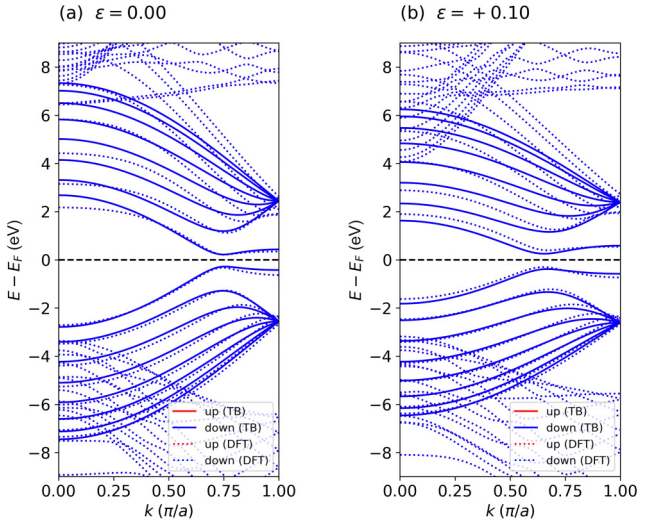

FIG. 4. Band structure of the 8-ZGNR obtained with the TB (solid line) and DFT (dotted line) approaches in the AFM configuration for (a) strain-free and (b) strain of +0.10 cases.

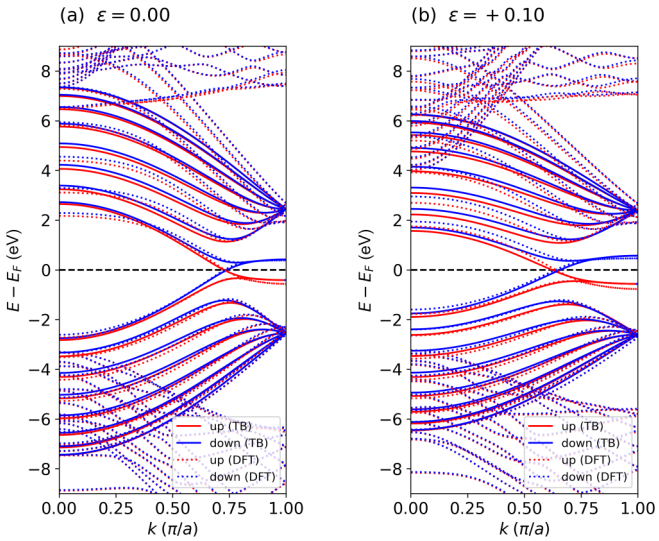

FIG. 5. Band structures of the 8-ZGNR obtained with the TB (solid line) and DFT (dotted line) approaches in the FM configuration for (a) strain-free and (b) strain of +0.10 cases.

We proceed analogously with the FM configuration of the 8-ZGNR. The band structure for the strain-free case is shown in Fig. 5(a). In the FM solution, the degeneracy of the up and down spin bands is broken. Now the system is gapless and the spin-up polarized edge band lies below the Fermi level, giving rise to a nonzero magnetic moment. The strained +0.10 case is shown in Fig. 5(b). Once again, the overall aspect of the bands remains similar with applied strain, with the bands becoming flatter. Remarkably, the edge bands are more separated in the strained situation compared to the strain-free case. The Fermi level lies always symmetrically between the edge bands. Consequently, this separation, along with the fact that the flatter portions of the bands are larger, implies that more spin-up states are occupied than in the strain-free case, thereby increasing the net magnetic moment.

B. H adatoms in pristine ZGNRs

We now consider the effect of H atoms adsorbed onto the ZGNR. For numerical calculations, an adatom is placed in a supercell that is three times wider than the basic unit cell, corresponding to a concentration of approximately 2% for $W = 8$. Additional concentrations will be considered later. In graphene, H adatoms are well known to induce a magnetic moment in the surrounding C atoms of the opposite sublattice, resulting in a characteristic triangular or $\sqrt{3} \times \sqrt{3}$ pattern around the defect [10]. Consequently, the magnetic moment of the system is modified.

We compute the adsorption of H adatoms using three methods: the vacancy-model approach, the Anderson impurity model, and DFT calculations. Both the vacancy-model approach and the Anderson impurity model are implemented within the TB framework, described in detail in Sec. II. Figure 6 presents the results obtained with these three methods, including the spatial distribution of the magnetic moment in the supercell and the corresponding band structure. Here, the

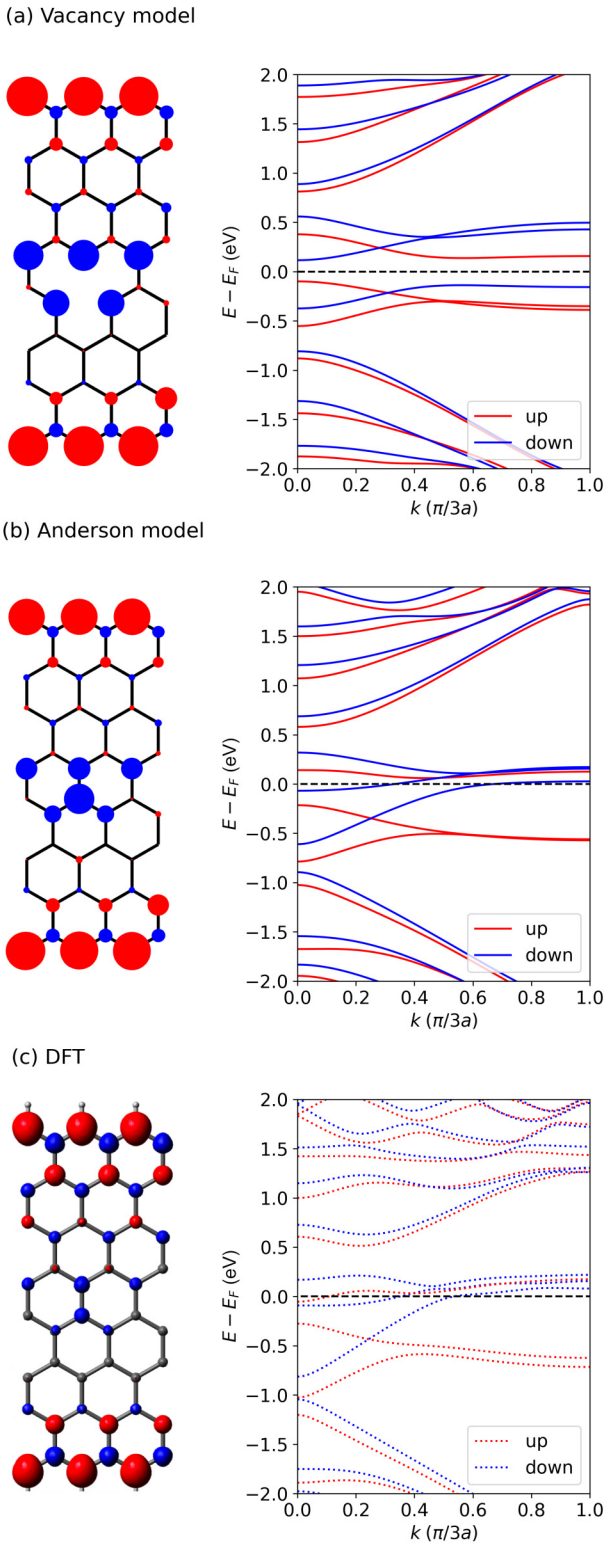

FIG. 6. Spatial distribution of the magnetic moment with an H adatom located at the fourth chain in 8-ZGNR supercell (with FM configuration at the edges) and the corresponding band structure computed using (a) the vacancy-model approach, (b) the Anderson impurity model, and (c) DFT calculations. Radii of the circles are proportional to the magnetic moment at each site, scaled by a smoothing factor to enhance visualization. Red circles indicate positive values and blue circles indicate negative ones.

H adatom is located at the central fourth chain and belongs to the sublattice opposite to that of its nearest (lower) edge. All methods reveal a very similar electronic spatial distribution, characterized by a noticeable triangular pattern of magnetic moments with negative values at the C atoms surrounding the H adatom, specifically those in the sublattice opposite to the defect, as anticipated. In both the Anderson model [see Fig. 6(b)] and the DFT results [see Fig. 6(c)], the H adatom also holds a prominent magnetic moment at the center of the triangle, differing from the empty space of the vacancy-model approach [Fig. 6(a)]. In these cases, the magnetic moment from the bonded C atom is hidden by the top H adatom. However, we have confirmed that no magnetic moment arises in this atom, making it irrelevant to the overall magnetic structure. Our choice of the fourth chain and edge-opposite sublattice for placing the H adatom is only motivated for a better visualization of the magnetic pattern. We have also explored other configurations with the H adatom at different positions and have found that the results are consistent with those presented here. Additionally, we show in Fig. S1 of the Supplemental Material [57] the case with the H adatom located at the fourth chain but same edge sublattice. Regarding the chain position, only when the H adatom is located just at the edges, and depending on its sublattice, it strongly interacts with the edge states, but this situation is in fact an edge modification, beyond the scope of our work.

We focus in this work on the FM configuration between the edges, since its metallic behavior offers a more suitable platform for studying and manipulating defect states by mechanical deformation of the ZGNR, in contrast to the gapped AFM solution. This solution in the presence of the H adatom is shown in Fig. S2 of the Supplemental Material [57] for completeness. The influence of edge states on the magnetic pattern of Fig. 6 is highly significant; they affect the defect state around the H adatom. To be specific, note the absence of a significant magnetic moment at the lower vertex of the triangular magnetic pattern. In an infinite graphene sheet, we would expect a negative magnetic moment at this atom, completing the well-known triangular magnetic pattern around the defect. This pattern is distorted due to its proximity to the lower edge of the ZGNR, where the electron exhibits spin-up polarization. Actually, the influence of the edge states is even more profound, determining the overall magnetic pattern. In contrast to the results for an isolated H adatom in bulk graphene, where the magnetic pattern typically exhibits spin-up polarization [2,10,49], here the pattern is forced into a spin-down configuration. We have found that this spin-down state is energetically the most favorable solution, differing by approximately 0.27 eV/atom from a solution with a spin-up defect pattern. Thus, the defect state is antiferromagnetically coupled to the edge states of the ZGNR, resulting in a ground state with a spin-down polarization.

With respect to the band structure, all models provide the same low-energy bands for $|E| < 1$ eV. For instance, in Fig. 6(a), two spin-up bands appear below the Fermi level, merging and flattening as k is closer to the boundary of the Brillouin zone. These bands correspond to the two spin-up edge states. Similarly, two equivalent spin-down bands are located above the Fermi level. Additionally, a single spin-down band near the Fermi level is related to the localized defect pattern, with its corresponding unoccupied counterpart. These six bands appear in all the models and methods chosen for this work. However, it is observed that the vacancy-model solution differs notably from DFT results, presenting an insulating gap and symmetric behavior around the Fermi level, in contrast to the metallic and asymmetric character of the DFT bands. In contrast, the bands obtained from the Anderson model exhibit a remarkable agreement with the DFT results. Then, we come to the conclusion that the common approach of simulating H adatoms as a vacant atomic site in the graphene lattice is not reliable enough [12,46,58]. As we have demonstrated, this approximation accurately describes the spatial distribution of magnetism, but fails to provide an accurate description of the band structure, most importantly, predicting an insulating behavior instead of metallic. In contrast, the Anderson impurity model, which is computationally less demanding than DFT calculations, offers a more accurate description of the electronic bands.

C. H adatoms in strained ZGNRs

Finally, we investigate the magnetic behavior of the H-adsorbed ZGNR in combination with strain. Due to the spatial symmetry breaking introduced by the adatom, it is more appropriate here to analyze the total magnetic moment M rather than focusing only on the edge magnetic moment, as we presented in Fig. 2. In Fig. 7(a), we show the total magnetic moment as a function of strain, from -0.05 to $+0.30$. The reason for this choice is to prevent out-of-plane deformations caused by high compressive strains, while providing an ample window for tensile strain. The figure shows that the magnetic moment increases under strain. Interestingly, unlike the smooth growth observed in Fig. 2, the magnetic moment exhibits a stepped behavior, characterized by plateaus where it remains constant. Remarkably, the magnetic moment has exactly odd integer values at these plateaus, with three distinct steps at $M(\mu_B) = 1, 3$, and 5. This behavior is observed in both the Anderson model and DFT calculations, with a reasonable good agreement between them.

To analyze the origin of the steps in the magnetic moment as a function of strain, we present the band structure for three representative strain values of -0.03 [see Fig. 7(b)], $+0.03$ [see Fig. 7(c)], and $+0.17$ [see Fig. 7(d)], which correspond to the first plateau, the transition region, and the second plateau, respectively. Again, the good agreement between the band structure obtained from the Anderson model and the DFT calculations is apparent. At strain -0.03, the bands exhibit half-metallic behavior. A half-metal is characterized by being an insulator for one spin orientation, while remaining metallic for the other [59]. As observed in Fig. 7(b), for spin-up polarization, the bands are filled and separated by a bandgap from the unoccupied bands. In contrast, the spin-down bands are partially occupied, showing a metallic behavior for this spin polarization. A central characteristic of the half-metallic systems is the quantized value of magnetization [59], which in our system manifests as the $M = \mu_B$ plateau. This arises because the system contains an integer number of $N_\uparrow$ spin-up electrons due to the filled bands, as well as an integer total number of electrons $N = N_\uparrow + N_\downarrow$ in the supercell, where $N_\downarrow$ is the number of spin-down electrons. Consequently, there

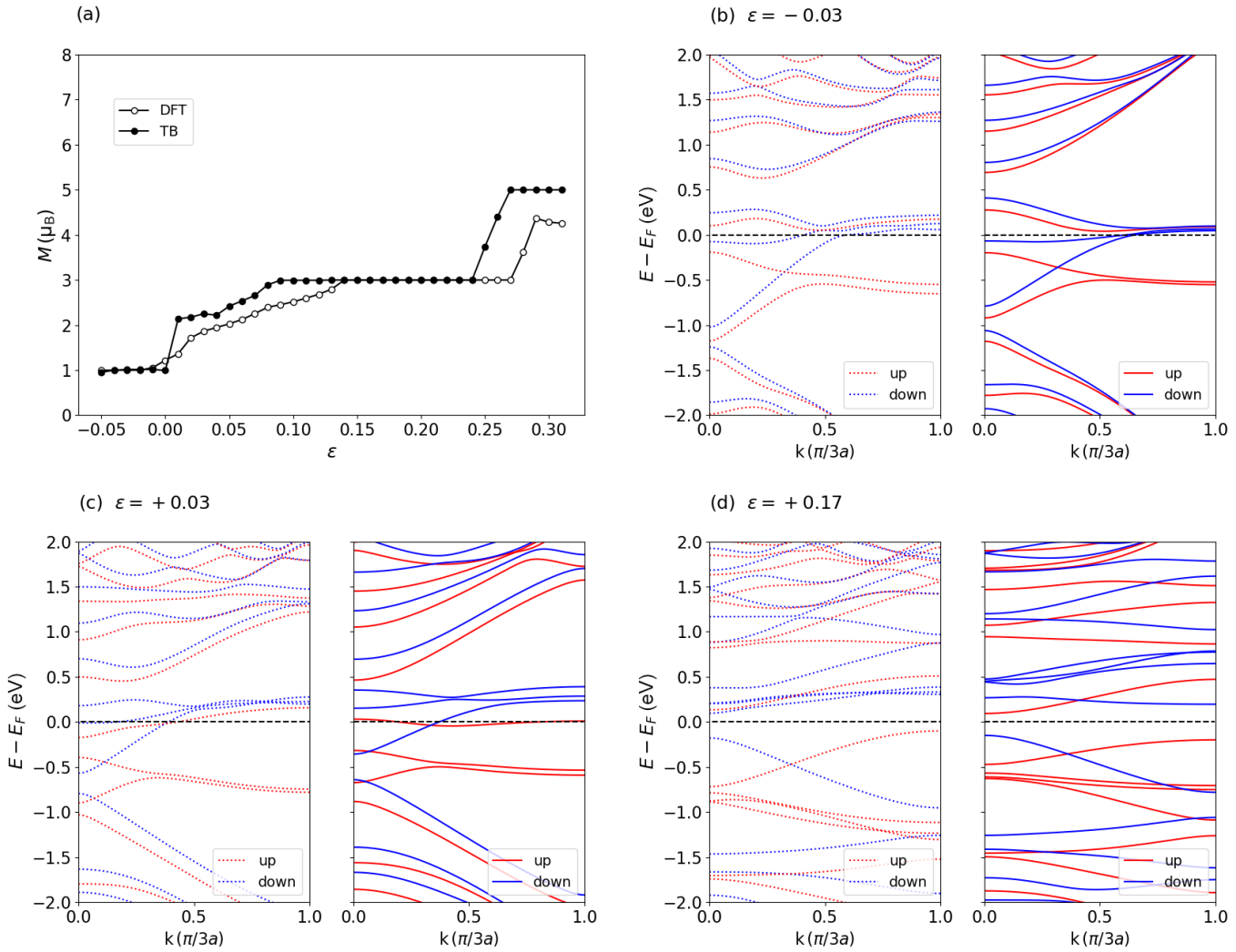

FIG. 7. (a) Total magnetic moment as a function of strain in the H-adsorbed 8-ZGNR supercell. Band structures obtained from DFT (dashed line) and TB (solid line) methods for strain values of (b) −0.03, (c) +0.03, and (d) +0.17, corresponding to the first plateau, the transition region, and second plateau, respectively.

must be an integer number $N_\downarrow$ of spin-down electrons even if the corresponding bands are partially filled. Comparing the DFT bands from Fig. 7(b) with the DFT strain-free adatom case depicted in Fig. 6(c), we observe that the bands are very similar. The key difference is that in the unstrained DFT case the spin-up defect band crosses the Fermi level near $k = 0$, departing from the half-metallic behavior. Therefore, the system undergoes a transition from half-metallic to being metallic for both spins, which explains why the magnetic moment deviates from the plateau at zero strain in Fig. 7(a) for the DFT calculation. In the strain-free TB results from Fig. 6(b), the spin-up band does not cross the Fermi level and the system remains half-metallic, where the transition to metallic occurs at +0.01 strain.

The region of noninteger growing magnetic moment between the first and second plateaus in Fig. 7(a) indicates the metallic behavior of the system at those strains, which is confirmed by the +0.03 strain bands [see Fig. 7(c)], where the Fermi level is crossed by both spin bands. The second plateau is explained with the help of Fig. 7(d), which depicts the bands for the strained ZGNR with $\epsilon = +0.17$, for which an integer $M = 3\ \mu_B$ magnetic moment is found in both the DFT and the TB model. The band structures obtained with both approaches display a bandgap for the two spins. The origin of this second quantized plateau differs from the previous one and stems from the integer number of occupied bands for both spin polarizations: The imbalance between the number of filled spin-up and spin-down bands gives rise to the integer value of the magnetic moment. The same situation occurs for the $M = 5\ \mu_B$ plateau. In the latter case, DFT calculations do not reach the plateau predicted by the TB approach for large strains, probably due to the substantial distortion effects caused by the huge strain values required to reach this plateau.

This steplike behavior in the magnetic moment also appears for other adatom concentrations, indicating that it is a general feature of H-adsorbed strained ZGNRs. Figure 8 presents the cases with lower H densities of 1.5% and 1.2%, in comparison with the previously discussed 2% case. The plateaus and the transition regions between them persist in all densities. Notably, the emergence of plateaus occurs at lower strain values as the H adatom concentration decreases. As a result, the lower $M = \mu_B$ plateau is not observed in the 1.5%

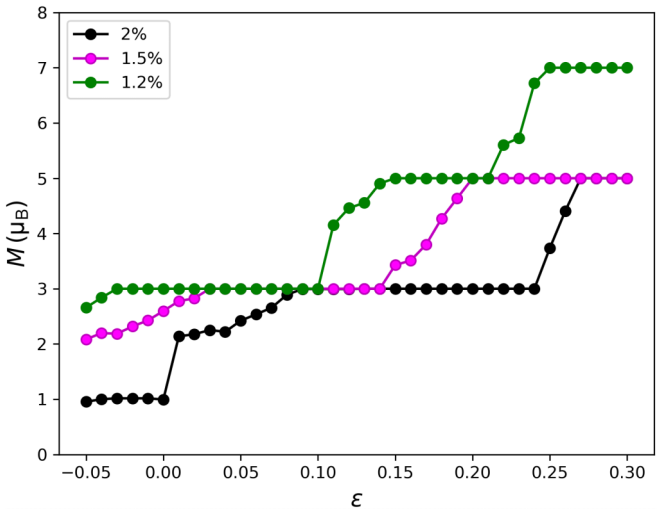

FIG. 8. Total magnetic moment as a function of strain in the H-adsorbed 8-ZGNR with different H concentrations.

and 1.2% cases within the strain range considered here. In contrast, an $M = 7\,\mu_B$ plateau emerges at the lowest density of 1.2%.

The previous results present intriguing possibilities for the systems studied in this work. First, half-metallic materials are highly desired for spintronic applications as a means to generate completely spin-polarized currents. The realization of half-metallicity in ZGNRs has already been predicted in different setups, such as the use of electric fields [22], edge modification [60], substitutional doping [61,62], or magnetic atom adsorption [63], typically transition metals. However, these situations tend to be experimentally more complex than the adsorption of H adatoms. Second, the appearance of quantized magnetic moments may hold potential for future magnetic applications, given that the required conditions are not exceedingly challenging, namely, the use of H adatoms, which are among the most common dopants. Furthermore, the observed dependence of the plateau positions on H density can be exploited to access the plateaus without requiring excessive strain values.

IV. CONCLUSIONS

In summary, we have investigated the effects of strain and H adatom adsorption on the magnetic properties of ZGNRs using a combination of TB models and DFT methods. A longitudinal strain applied along the ZGNRs makes the magnetic moments in both FM and AFM configurations increase progressively with strain, achieving a significant growth rate. This enhancement in magnetic moment is attributed to strain-induced modifications in the band structure and has a smooth behavior. Our TB model shows excellent agreement with DFT calculations and enabled us to study much larger systems with reduced computational effort compared to DFT calculations. We have explored the effects of H adatoms on ZGNRs with different computational approaches. We found that modeling H adatoms as vacancies does not accurately capture the band structure, leading to misleading conclusions. The Anderson impurity model, however, yields excellent agreement with the DFT-derived band structure. The magnetic configuration of H adatoms is largely influenced by the edges of the ZGNR, where the ground state exhibits AFM coupling between the defect and the edges. Interestingly, H adatoms induce a half-metallic character in ZGNRs. When combined with strain, it induces robust, quantized magnetic moments, characterized by distinct plateaus of integer values with varying strain. While the first plateau induced by smooth strain arises from the half-metallic character, subsequent plateaus observed at higher strains emerge due to the transition to a gapped state. These findings offer valuable guidelines for the manipulation of magnetism in ZGNRs and advance our capabilities for tuning magnetic properties in two-dimensional materials.

ACKNOWLEDGMENTS

This work was supported by the Spanish Ministry of Science and Innovation (Grants No. PID2022-136285NB-C31 and No. PID2022-136636OB-I00). We also acknowledge the support from the "(MAD2D-CM)-UCM" project funded by Comunidad de Madrid, by the Recovery, Transformation and Resilience Plan, and by NextGenerationEU from the European Union. We also acknowledge the computational resources and assistance provided by the Centro de Computación de Alto Rendimiento CCAR-UNED and Servicio de SuperComputación SSC-UCLM.

DATA AVAILABILITY

The data supporting this study's findings are available within the article.

[1] O. Volnianska and P. Boguslawski, Magnetism of solids resulting from spin polarization of *p* orbitals, J. Phys.: Condens. Matter **22**, 073202 (2010).

[2] O. V. Yazyev, Emergence of magnetism in graphene materials and nanostructures, Rep. Prog. Phys. **73**, 056501 (2010).

[3] D. G. de Oteyza and T. Frederiksen, Carbon-based nanostructures as a versatile platform for tunable π-magnetism, J. Phys.: Condens. Matter **34**, 443001 (2022).

[4] A. Avsar, H. Ochoa, F. Guinea, B. Özyilmaz, B. J. Van Wees, and I. J. Vera-Marun, *Colloquium*: Spintronics in graphene and other two-dimensional materials, Rev. Mod. Phys. **92**, 021003 (2020).

[5] W. Han, R. K. Kawakami, M. Gmitra, and J. Fabian, Graphene spintronics, Nat. Nanotechnol. **9**, 794 (2014).

[6] O. V. Yazyev, Hyperfine interactions in graphene and related carbon nanostructures, Nano Lett. **8**, 1011 (2008).

[7] H. Min, J. Hill, N. A. Sinitsyn, B. Sahu, L. Kleinman, and A. H. MacDonald, Intrinsic and rashba spin-orbit interactions in graphene sheets, Phys. Rev. B **74**, 165310 (2006).

[8] D. Huertas-Hernando, F. Guinea, and A. Brataas, Spin-orbit coupling in curved graphene, fullerenes, nanotubes, and nanotube caps, Phys. Rev. B **74**, 155426 (2006).

[9] M. Drögeler, C. Franzen, F. Volmer, T. Pohlmann, L. Banszerus, M. Wolter, K. Watanabe, T. Taniguchi, C. Stampfer, and B. Beschoten, Spin lifetimes exceeding 12 ns in graphene nonlocal spin valve devices, Nano Lett. **16**, 3533 (2016).

[10] O. V. Yazyev and L. Helm, Defect-induced magnetism in graphene, Phys. Rev. B **75**, 125408 (2007).

[11] O. V. Yazyev, Magnetism in disordered graphene and irradiated graphite, Phys. Rev. Lett. **101**, 037203 (2008).

[12] J. J. Palacios, J. Fernández-Rossier, and L. Brey, Vacancy-induced magnetism in graphene and graphene ribbons, Phys. Rev. B **77**, 195428 (2008).

[13] H. Ohldag, T. Tyliszczak, R. Höhne, D. Spemann, P. Esquinazi, M. Ungureanu, and T. Butz, π-electron ferromagnetism in metal-free carbon probed by soft X-Ray dichroism, Phys. Rev. Lett. **98**, 187204 (2007).

[14] J. Barzola-Quiquia, P. Esquinazi, M. Rothermel, D. Spemann, T. Butz, and N. García, Experimental evidence for two-dimensional magnetic order in proton bombarded graphite, Phys. Rev. B **76**, 161403 (2007).

[15] M. M. Ugeda, I. Brihuega, F. Guinea, and J. M. Gómez-Rodríguez, Missing atom as a source of carbon magnetism, Phys. Rev. Lett. **104**, 096804 (2010).

[16] H. González-Herrero, J. M. Gómez-Rodríguez, P. Mallet, M. Moaied, J. J. Palacios, C. Salgado, M. M. Ugeda, J.-Y. Veuillen, F. Yndurain, and I. Brihuega, Atomic-scale control of graphene magnetism by using hydrogen atoms, Science **352**, 437 (2016).

[17] P. Merino, H. Santos, A. L. Pinardi, L. Chico, and J. A. Martin-Gago, Atomically-resolved edge states on surface-nanotemplated graphene explored at room temperature, Nanoscale **9**, 3905 (2017).

[18] W. Jaskólski, A. Ayuela, M. Pelc, H. Santos, and L. Chico, Edge states and flat bands in graphene nanoribbons with arbitrary geometries, Phys. Rev. B **83**, 235424 (2011).

[19] L. Pisani, J. A. Chan, B. Montanari, and N. M. Harrison, Electronic structure and magnetic properties of graphitic ribbons, Phys. Rev. B **75**, 064418 (2007).

[20] J. J. Palacios, J. Fernández-Rossier, L. Brey, and H. A. Fertig, Electronic and magnetic structure of graphene nanoribbons, Semicond. Sci. Technol. **25**, 033003 (2010).

[21] H. Santos, L. Chico, and L. Brey, Carbon nanoelectronics: Unzipping tubes into graphene ribbons, Phys. Rev. Lett. **103**, 086801 (2009).

[22] Y.-W. Son, M. L. Cohen, and S. G. Louie, Half-metallic graphene nanoribbons, Nature (London) **444**, 347 (2006).

[23] F. Muñoz Rojas, J. Fernández-Rossier, and J. J. Palacios, Giant magnetoresistance in ultrasmall graphene based devices, Phys. Rev. Lett. **102**, 136810 (2009).

[24] W. Y. Kim and K. S. Kim, Prediction of very large values of magnetoresistance in a graphene nanoribbon device, Nat. Nanotechnol. **3**, 408 (2008).

[25] M. Zeng, L. Shen, M. Zhou, C. Zhang, and Y. Feng, Graphene-based bipolar spin diode and spin transistor: Rectification and amplification of spin-polarized current, Phys. Rev. B **83**, 115427 (2011).

[26] P. Vancsó, I. Hagymási, and L. Tapasztó, A magnetic phase-transition graphene transistor with tunable spin polarization, 2D Mater. **4**, 024008 (2017).

[27] X. Li, X. Wang, L. Zhang, S. Lee, and H. Dai, Chemically derived, ultrasmooth graphene nanoribbon semiconductors, Science **319**, 1229 (2008).

[28] J. Bai, X. Duan, and Y. Huang, Rational fabrication of graphene nanoribbons using a nanowire etch mask, Nano Lett. **9**, 2083 (2009).

[29] B. Huang, F. Liu, J. Wu, B.-L. Gu, and W. Duan, Suppression of spin polarization in graphene nanoribbons by edge defects and impurities, Phys. Rev. B **77**, 153411 (2008).

[30] P. Ruffieux, S. Wang, B. Yang, C. Sánchez-Sánchez, J. Liu, T. Dienel, L. Talirz, P. Shinde, C. A. Pignedoli, D. Passerone *et al.*, On-surface synthesis of graphene nanoribbons with zigzag edge topology, Nature (London) **531**, 489 (2016).

[31] J. Brede, N. Merino-Díez, A. Berdonces-Layunta, S. Sanz, A. Domínguez-Celorrio, J. Lobo-Checa, M. Vilas-Varela, D. Peña, T. Frederiksen, J. I. Pascual *et al.*, Detecting the spin-polarization of edge states in graphene nanoribbons, Nat. Commun. **14**, 6677 (2023).

[32] M. Pizzochero and E. Kaxiras, Hydrogen atoms on zigzag graphene nanoribbons: Chemistry and magnetism meet at the edge, Nano Lett. **22**, 1922 (2022).

[33] F. Miao, S.-J. Liang, and B. Cheng, Straintronics with van der Waals materials, npj Quantum Mater. **6**, 59 (2021).

[34] V. M. Pereira, A. C. Neto, and N. Peres, Tight-binding approach to uniaxial strain in graphene, Phys. Rev. B **80**, 045401 (2009).

[35] M. Settnes, S. R. Power, M. Brandbyge, and A.-P. Jauho, Graphene nanobubbles as valley filters and beam splitters, Phys. Rev. Lett. **117**, 276801 (2016).

[36] D. Zhai and N. Sandler, Local versus extended deformed graphene geometries for valley filtering, Phys. Rev. B **98**, 165437 (2018).

[37] G. Yang, B. Li, W. Zhang, M. Ye, and T. Ma, Strain-tuning of edge magnetism in zigzag graphene nanoribbons, J. Phys.: Condens. Matter **29**, 365601 (2017).

[38] R. Farghadan, Mechanical spin splitting in zigzag graphene nanoribbons, Phys. Rev. B **110**, 195411 (2024).

[39] W. Jaskólski, L. Chico, and A. Ayuela, Divacancy-induced ferromagnetism in graphene nanoribbons, Phys. Rev. B **91**, 165427 (2015).

[40] G. G. Naumis, S. Barraza-Lopez, M. Oliva-Leyva, and H. Terrones, Electronic and optical properties of strained graphene and other strained 2D materials: A review, Rep. Prog. Phys. **80**, 096501 (2017).

[41] F. Liu, P. Ming, and J. Li, *Ab initio* calculation of ideal strength and phonon instability of graphene under tension, Phys. Rev. B **76**, 064120 (2007).

[42] D. Sánchez-Portal, E. Artacho, J. M. Soler, A. Rubio, and P. Ordejón, *Ab initio* structural, elastic, and vibrational properties of carbon nanotubes, Phys. Rev. B **59**, 12678 (1999).

[43] J. Fernández-Rossier and J. J. Palacios, Magnetism in graphene nanoislands, Phys. Rev. Lett. **99**, 177204 (2007).

[44] D. Gunlycke, D. A. Areshkin, J. Li, J. W. Mintmire, and C. T. White, Graphene nanostrip digital memory device, Nano Lett. **7**, 3608 (2007).

[45] J. Fernández-Rossier, Prediction of hidden multiferroic order in graphene zigzag ribbons, Phys. Rev. B **77**, 075430 (2008).

[46] D. Soriano, F. Muñoz Rojas, J. Fernández-Rossier, and J. J. Palacios, Hydrogenated graphene nanoribbons for spintronics, Phys. Rev. B **81**, 165409 (2010).

[47] R. Ribeiro, V. M. Pereira, N. Peres, P. Briddon, and A. C. Neto, Strained graphene: Tight-binding and density functional calculations, New J. Phys. **11**, 115002 (2009).

[48] I. Sánchez-Ramírez, Y. Baba, L. Chico, and F. Domínguez-Adame, Impact of electron-electron interactions on the thermoelectric efficiency of graphene quantum point contacts, Phys. Rev. B **106**, 045129 (2022).

[49] J. O. Sofo, G. Usaj, P. S. Cornaglia, A. M. Suarez, A. D. Hernández-Nieves, and C. A. Balseiro, Magnetic structure of hydrogen-induced defects on graphene, Phys. Rev. B **85**, 115405 (2012).

[50] T. Wehling, S. Yuan, A. Lichtenstein, A. Geim, and M. Katsnelson, Resonant scattering by realistic impurities in graphene, Phys. Rev. Lett. **105**, 056802 (2010).

[51] D. Choe, J. Bang, and K.-J. Chang, Electronic structure and transport properties of hydrogenated graphene and graphene nanoribbons, New J. Phys. **12**, 125005 (2010).

[52] J. M. Soler, E. Artacho, J. D. Gale, A. García, J. Junquera, P. Ordejón, and D. Sánchez-Portal, The SIESTA method for *ab initio* order-*n* materials simulation, J. Phys.: Condens. Matter **14**, 2745 (2002).

[53] B. Hammer, L. B. Hansen, and J. K. Nørskov, Improved adsorption energetics within density-functional theory using revised Perdew-Burke-Ernzerhof functionals, Phys. Rev. B **59**, 7413 (1999).

[54] H. Zhao, K. Min, and N. R. Aluru, Size and chirality dependent elastic properties of graphene nanoribbons under uniaxial tension, Nano Lett. **9**, 3012 (2009).

[55] C. Lee, X. Wei, J. W. Kysar, and J. Hone, Measurement of the elastic properties and intrinsic strength of monolayer graphene, Science **321**, 385 (2008).

[56] H. H. Pérez-Garza, E. W. Kievit, G. F. Schneider, and U. Staufer, Highly strained graphene samples of varying thickness and comparison of their behaviour, Nanotechnology **25**, 465708 (2014).

[57] See Supplemental Material at http://link.aps.org/supplemental/10.1103/6tny-vt8q for other configurations not considered in the main text.

[58] D. Soriano, D. Van Tuan, S. M. Dubois, M. Gmitra, A. W. Cummings, D. Kochan, F. Ortmann, J.-C. Charlier, J. Fabian, and S. Roche, Spin transport in hydrogenated graphene, 2D Mater. **2**, 022002 (2015).

[59] W. E. Pickett and J. S. Moodera, Half metallic magnets, Phys. Today **54**(5), 39 (2001).

[60] E.-j. Kan, Z. Li, J. Yang, and J. Hou, Half-metallicity in edge-modified zigzag graphene nanoribbons, J. Am. Chem. Soc. **130**, 4224 (2008).

[61] X. Hu, N. Wan, L. Sun, and A. V. Krasheninnikov, Semiconductor to metal to half-metal transition in PT-embedded zigzag graphene nanoribbons, J. Phys. Chem. C **118**, 16133 (2014).

[62] S. Dutta, A. K. Manna, and S. K. Pati, Intrinsic half-metallicity in modified graphene nanoribbons, Phys. Rev. Lett. **102**, 096601 (2009).

[63] M. R. Rezapour, G. Lee, and K. S. Kim, A high performance n-doped graphene nanoribbon based spintronic device applicable with a wide range of adatoms, Nanoscale Adv. **2**, 5905 (2020).